The Influence of Device Physical Parameters on HEMT Large-Signal Characteristics

MATTHIAS WEISS, STUDENT MEMBER, IEEE, AND DIMITRIS PAVLIDIS, SENIOR MEMBER, IEEE

Abstract—**The small- and large-signal high-frequency characteristics of submicron HEMT's are analyzed by taking into account parasitic effects such as parallel conduction, fringing capacitances, and substrate leakage. The dependence of large-signal properties on device physical parameters is reported. This includes device gate length, donor layer thickness and doping, and spacer thickness. Satisfactory agreement is shown to exist between theoretically and experimentally obtained device characteristics.**

NOMENCLATURE

a_i	Parameters for fitting $E_f - n_s$.
C_{gs}, C_{gd}	Gate–source and gate–drain capacitance.
d_G	Depth of substrate charge.
d_0	Thickness of the doped AlGaAs layer.
E	Electric field.
E_f	Fermi energy.
f	$=10^{-15}$: normalizing factor.
F_c	Critical electric field.
F_0	Electric field in $v(E)$ formula.
G_{ds}	Output conductance.
g_m	Transconductance.
G_{gdi}	Intrinsic gate–drain conductance.
G_{sub}	Substrate conductance.
I_d	Drain–source current.
I_{g0}	Reverse diode current.
$I_{\max}$	Maximum drain–source current.
K_h, K_n	Substrate injection parameters.
K_0	Integration constant.
L_g	Gate length.
L_{GS}, L_{GD}	Gate–source and gate–drain spacing.
L_1, L_2	Length of linear and saturated regions.
N_d	Doping concentration.
n_s	Concentration of two-dimensional electron gas.
n_{sat}	Saturated value of n_s.
P	Adjusting parameter.
q	1.602×10^{-19} A sec: electron charge.
$Q_g, Q_{ns}, Q_{GS}, Q_{GD}, Q_T$	Transistor charges.
R_i	Intrinsic gate resistance.
R_s, R_d	Parasitic source, drain resistances.
R_{ds}	$1/G_{ds}$.
r_{GS}, r_{GD}	Lengths of regions with parasitic charges.
v	Electron velocity.
v_s	Saturated electron velocity.
V_{fi}	Schottky barrier.
V_{sr}	Voltage drop across saturated region.
V_e	Effective channel potential.
V_{ea}	V_e at the onset of electron gas modulation.
V_{eb}	V_e at the onset of velocity saturation.
V_d	Distance-dependent drain–source voltage.
V_{dl}	Intrinsic drain–source voltage across gate L_g.
V_{ds}	External drain–source bias voltage.
V_g	Gate–source voltage.
V_{gi}, V_{gdi}	Intrinsic gate–source and gate–drain voltage.
W_{gs}, W_{gd}	Dimensions of regions with parasitic charges.
W_g	Width of parasitic "MESFET-channel" in HEMT.
z	Distance along the $S-D$ axis.
ε_2	Relative dielectric constant of AlGaAs.
α_1, α_2	Angles for definition of parasitic edge regions.
τ	Transit time constant.
μ	Electron mobility.
ΔE_c	Bandgap discontinuity.
$a, b, \beta, \gamma, C_0, C_1, C_2, V_{e1}, V_{e2}$	Constants depending on device geometry and material parameters.

Manuscript received April 24, 1987; revised August 31, 1987. This work was supported in part by the U.S. Army Research Office under Grant DAAL03-87-U-007 and by the Wright Patterson Air Force Base under Contract F33615-87-C-1406

The authors are with the Center for High Frequency Microelectronics, Solid State Electronics Laboratory, University of Michigan, Ann Arbor, MI 48109-2122.

IEEE Log Number 8717975.

I. INTRODUCTION

HIGH ELECTRON MOBILITY TRANSISTORS (HEMT's) have demonstrated excellent small-signal and noise characteristics [1], [3], [6]. Their use in power applications has also proved to be advantageous for high-frequency operation with large power-added efficiencies [7].

Although several works treated the dc characteristics of HEMT's [1]–[5], [8], [9], the high-frequency behavior was mainly analyzed experimentally [10], [11]. This paper presents a physical analysis of HEMT's capable of providing information about their high-freuqency performance. A triangular well approximation is used for the two-dimensional electron gas, and the dependence of its sheet density n_s on the Fermi level E_f is described by an

0018-9480/88/0200-0239$01.00

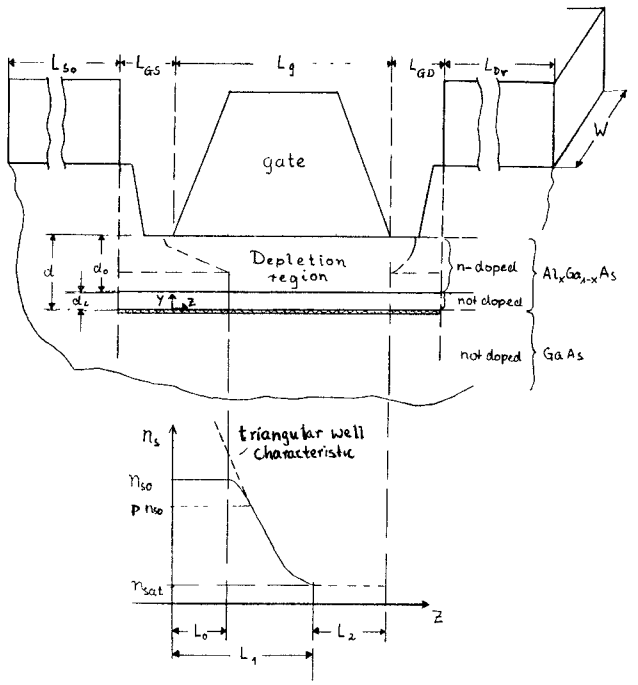

Fig. 1. Cross section of the investigated HEMT structure with electron gas concentration profile. L_{s0}, L_{dr} = source, drain pad length; L_{GS}, L_{GD} = gate–source and gate–drain spacing; W = gate width; L_g = gate length; d = donor (AlGaAs) and spacer layer total thickness; d_t = spacer layer thickness; d_0 = AlGaAs donor layer thickness; n_{s0} = equilibrium value of n_s; n_{sat} = saturated value of n_s.

interpolation function which describes accurately the nonlinear $n_s - E_f$ characteristics.

The one-dimensional analysis of the devices is based on analytical expressions and gives very satisfactory results on the current–voltage characteristics and the voltage dependence of device charges (Section II). Parasitic, "MESFET-like" parallel conduction in the doped HEMT layer is also included.

Using the values of the derived physical parameters, the high-frequency characteristics could be predicted under small-signal operating conditions (Section III). The validity of the model is checked by comparing it to experimentally obtained high-frequency data (Section IV). Using the method previously reported by the authors for power MESFET analysis [12]–[14], the large-signal HEMT properties could be investigated (Section V). Gate–drain avalanche [15], [16], and breakdown current [17] are included in the analysis. The gate–source diode forward operation occurring at large input levels is also considered. Section V also examines the dependence of large-signal characteristics on physical parameters, in particular on gate length, donor layer thickness and doping, and spacer thickness.

Limitations of this model arise from its one-dimensional characteristics and the fact that surface states are neglected. Although experimental data prove the validity of the model up to 26 GHz, distributed effects will have to be considered above these frequencies. The present model is based on a triangular well approximation but can be easily expanded to any other form of energy band discontinuity.

II. HEMT Analysis Based on Physical Parameters

The cross section of the investigated HEMT structure is shown in Fig. 1 together with the physical parameters used in the theory presented below. The analysis includes the calculation of $I-V$ characteristics and the voltage dependence of device charges.

A. $I-V$ Characteristics

The drain current can be evaluated by the following equation:

$$I_d = q n_s(z) W v(z). \tag{1}$$

For given current I_d, the drain voltage $V_d(z)$ can be calculated by integration of (1) over the distance z. This can be performed analytically if the electron velocity $v(z) = v(E(z))$ is given by a two-piece $v-E$ model:

$$v(E) = \begin{cases} \mu \dfrac{E}{1+E/F_0} & E < F_c \\ v_s & E > F_c \end{cases}$$

$$F_0 = F_c v_s/(\mu F_c - v_s) \qquad E = dV_d/dz. \tag{2}$$

F_c is the saturation field, v_s the saturation velocity, and μ the mobility.

The concentration of the two-dimensional electron gas $n_s(z) = n_s(V_e(z))$ can be obtained from

$$n_s(V_e) = \begin{cases} a + bV_e + (b^2V_e^2 + \beta V_e + \gamma) & V_e < V_{e1} \\ c_0 + c_1 V_e + c_2 V_{e2} & V_{e1} \leqslant V_e < {}_{e2} \\ f n_{s0} & V_{e2} \leqslant V_e. \end{cases} \tag{3}$$

Here n_{s0} is the equilibrium concentration of the two-dimensional electron gas, and f is a normalizing factor set to $f = 10^{-15}$. The constants a, b, β, γ, c_0, c_1, c_2, V_{e1}, and V_{e2} depend on device geometry and material parameters and are evaluated as described in Appendix I. V_e is the effective channel potential given by [1]

$$V_e = V_g - V_d(z) - V_{fi} + \Delta E_c + q N_d d_0^2/(2\varepsilon_2). \tag{4}$$

The constants $a, b, \cdots$ of (3) can be derived if the relation between Fermi energy and electron gas concentration is known. The following relation is used:

$$E_f = \frac{a_0 + a_1(fn_s) + a_2(fn_s)^2}{(fn_s) + a_3}. \tag{5}$$

Equation (5) approximates better the results of E_f versus n_s characteristics than simple linear functions ([3], [4]). The parameters a_i necessary to fit the triangular $E_f - n_s$ characteristics at a temperature of 300 K are given in Appendix I. Curve fitting of this type can also be applied to more accurate numerically calculated E_f versus n_s data.

The mathematical transformation of (1) using (2) leads to

$$I_d\, dz = (W q n_s \mu - I_d/F_0)\, dV_d. \tag{6}$$

Equation (6) can be integrated along the channel (z axis) until the saturation velocity v_s is reached at $z = L_1$:

$$I_d L_1 = qW\mu \int_{V_{eb}}^{V_{ea}} n_s \, dV_e + I_d(V_{eb} - V_{ea})/F_0 \tag{7a}$$

$$V_{eb} = V_g - V_d(z = L_1) - V_{fi} + \Delta E_c + qN_d d_0^2/(2\varepsilon_2) \tag{7b}$$

$$V_{ea} = V_g - V_d(z = 0) - V_{fi} + \Delta E_c + qN_d d_0^2/(2\varepsilon_2). \tag{7c}$$

V_e is given in (4) and the integral $\int n_s \, dV_e$ is calculated in Appendix II. If the bias voltages are chosen such that the carriers do not attain the saturation velocity, L_1 of (7) must be replaced by L_g. $V_d(z = L_g)$ and $V_d(z = 0)$ can be obtained from

$$V_d(z = 0) = R_s I_d \tag{8a}$$

$$V_d(z = L_g) = V_{ds} - R_d I_d. \tag{8b}$$

Given V_{ds} and V_g, (7) can then be iteratively solved for I_d. For large drain bias, the velocity usually reaches saturation. The saturated electron gas concentration n_{sat} can then be determined using $v(z) = v_s$ in (1):

$$n_{\text{sat}} = I_d/(qWv_s). \tag{9}$$

For $z > L$, n_{sat} remains constant due to the constant carrier velocity.

The voltage drop across the nonsaturated part of the channel $V_d(z = L_1)$ can now be obtained by solving (3) and (4) for V_d:

$$V_e(z = L_1) = \begin{cases} -c_1/(2c_2) - \sqrt{(c_1/[2c_2])^2 - (c_0 - fn_{\text{sat}})/c_2} & \text{for } pn_{s0} < n_{\text{sat}} < n_{s0} \\ \dfrac{qd_0 fn_{\text{sat}}}{f\varepsilon_2} + \dfrac{a_0 + a_1 fn_{\text{sat}} + a_2(fn_{\text{sat}})^2}{fn_{\text{sat}} + a_3} & \text{for } n_{\text{sat}} < pn_{s0} \end{cases} \tag{10a}$$

$$V_d(z = L_1) = \Delta E_c - V_{fi} + V_g - V_e(L_1) + qN_d d_0^2/(2\varepsilon_2) \tag{10b}$$

Here p is a parameter necessary to ensure a smooth transition from the n_{s0} value to the variable $n_s - V_d(z)$ region predicted by (5) (see Fig. 1) and was set to be 0.75.

The length L_1 of the "linear" channel region is calculated by solving (7):

$$L_1 = \frac{qW\mu \int_{V_{eb}}^{V_{ea}} n_s \, dV_e + I_d(V_{eb} - V_{ea})/F_0}{I_d}. \tag{11}$$

The voltage drop V_{sr} across the saturated HEMT region of length $L_2 = L_g - L_1$ is evaluated by solving a one-dimensional Poisson equation in this region as described in [5] and [6]:

$$V_{sr} = k_0 I_d L_2^2/2 + F_c L_2 \tag{12}$$

where

$$k_0 = \frac{1}{\varepsilon W d_G v_s}.$$

The voltage V_{ds} across the entire HEMT structure is now obtained by introducing (8), (10), and (12) in

$$V_{ds} = V_d(L_1) + I_{ds} R_d. \tag{13}$$

Equation (13) can be iteratively solved for I_d if the bias voltages V_{ds} and V_g are given.

In order to obtain the I–V characteristics of a device, parasitic currents through the substrate also have to be taken into account. The substrate conduction depends on background doping and carrier injection. In dc operation, these effects are partially compensated by the influence of slowly responding traps, and the current can be modeled by carrier injection only. The substrate conductance is then assumed to be approximately proportional to the saturated electron gas concentration n_{sat} and inversely proportional to the gate length:

$$G_{\text{sub}} = k_n(n_{\text{sat}}/n_{s0})(1/L_g). \tag{14}$$

Under these conditions, the substrate current is given by

$$I_{\text{sub}} = G_{\text{sub}} V_{dl}$$
$$V_{dl} = V_{ds} - (R_s + R_d) I_d. \tag{15}$$

In high-frequency operation, additional substrate currents may flow due to the absence of traps. These are modeled by an additional conductance term, resulting in a new conductance parameter $G_{\text{sub}\,h}$:

$$G_{\text{sub}\,h} = G_{\text{sub}} + k_h/L_g. \tag{16}$$

The substrate parameters k_h and k_n depend on the material and may vary from one device to the other.

The influence of parasitic MESFET operation has been considered for the estimation of device charges only (Section II-B-2). It is not important for I–V calculations of HEMT's biased for large-signal operation since the n-AlGaAs donor channel is then usually pinched off.

B. Voltage Dependence of Device Charges

The voltage-controlled charge of a HEMT originates from the two-Dimensional Electron Gas layer (2-DEG layer) under the channel and the parasitic regions extending outside the gate edges (see Fig. 2). Two different cases of operation are considered.

1) Normal HEMT Operation: Here, the gate voltage can control the electron gas and no parasitic MESFET channel exists between the gate and the 2-DEG layer (Fig. 2(a)). The modulated charge Q_{ns} of the 2-DEG layer can be obtained from

$$Q_{ns} = -Wq \int_0^{L_g} n_s(z) \, dz$$
$$= -\left(Wq \int_0^{V_e(L_1)} n_s(V_e)(dz/dV_e) \, dV_e + WqL_2 n_{\text{sat}} \right). \tag{17}$$

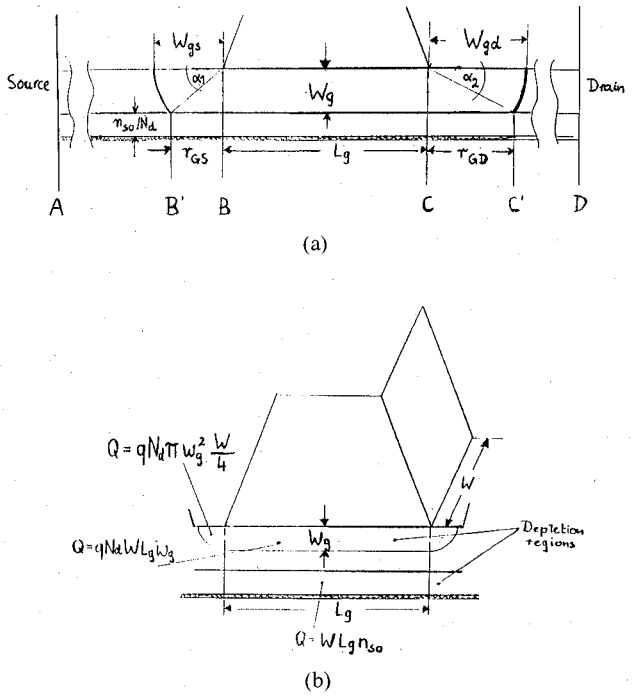

Fig. 2. HEMT cross section defining region with parasitic charges for (a) normal operation and (b) parasitic MESFET operation. W_{gs}, W_{gd} = width of region with parasitic charges; W_g = thickness of parasitic MESFET layer; r_{GS}, r_{GD} = depleted parasitic edge regions; n_{s0}/N_d = depletion due to electron gas.

The evaluation of the integrals of (17) is shown in Appendix II.

In addition to Q_{ns}, parasitic charges can be present in the device. These are associated with the regions outside the gate edges and originate from the 2-DEG channel and the depleted donor layer. The shape of these fringing regions is approximated by a circular section [18], [19] above the depleted region contributing to the 2-DEG electrons. Between the interface of the fringing and depleted regions (points B', C' of fig. 2(a)) and source or drain contacts (points A, D), the electron gas is not affected by the drain potential and has an equilibrium concentration n_{s0}. Between points $B'-B$ and $C'-C$ (Fig. 2(a)), the electron gas concentration decreases with channel potential until it reaches the concentrations $n_s = n_s(z = 0)$ or $n_s = n_s(z = L_g)$ at the source and drain side of the gate, respectively (points B, C). The n_s decrease in the $B'-B$, $C'-C$ regions can be assumed to be linear with the distance z. The total charge of these regions is then given by

$$Q_{GS} = -\left(qn_{s0}L_{GS}W - \left(n_{s0} - n_s(z=0)\right)/2r_{GS}Wq\right) \quad (18a)$$

$$Q_{GD} = -\left(qn_{s0}L_{GD}W - \left(n_{s0} - n_s(z=L_g)\right)/2r_{GD}Wq\right). \quad (18b)$$

The r_{GS} and r_{GD} lengths (Fig. 2(a)) are calculated as follows:

$$r_{GS(GD)}^2 = W_{gs(gd)}^2 - W_g^2. \quad (19a)$$

W_{gd} and W_{gs} are bias dependent and can be obtained from Schottky theory:

$$W_{gs(gd)} = \sqrt{2\varepsilon_2\left(V_{gs(gd)} - V_{fi}\right)/(qN_d)}. \quad (19b)$$

W_g is determined from the thickness n_{s0}/N_d of the depleted zone providing the 2-DEG gas ([1], [3], [4]) and the donor layer d_0:

$$W_g = d_0 - (n_{s0}/N_d). \quad (20)$$

The charges of the remaining AlGaAs regions can also be calculated by

$$Q_g = \left(\alpha_1 W_{gs}^2 + r_{GS}W_g/2 + r_{GD}W_g/2 + \alpha_2 W_{gd}^2 + W_g L_g\right)WqN_d$$
$$\alpha_1 = \pi/4 - \arccos\left(W_g/W_{gs}\right)$$
$$\alpha_2 = \pi/4 - \arccos\left(W_g/W_{gd}\right). \quad (21)$$

For given bias voltages, the total modulated charge Q_t is finally obtained:

$$Q_t = Q_{ns} + Q_{GS} + Q_{GD} + Q_g. \quad (22)$$

2) Parasitic MESFET Operation: Here, the gate potential does not control the electron gas concentration (Fig. 2(b)). The charge Q_{ns} in the 2-DEG layer is determined by the equilibrium electron gas concentration:

$$Q_{ns} = -\left(L_{GS} + L_g + L_{GD}\right)qn_{s0}W. \quad (23a)$$

The charge of the parasitic MESFET is bias dependent and given by

$$Q_g = \left(\pi W_{gs}/2 + W_g L_g\right)qN_d W. \quad (23b)$$

The total charge can again be obtained from

$$Q_t = Q_{ns} + Q_g. \quad (24)$$

III. High Frequency Characteristics

The small-signal high-frequency HEMT characteristics can be predicted from the equivalent circuit of Fig. 3. The elements g_m, $G_{ds} = 1/R_{ds}$, C_{gs}, C_{dg}, τ, and R_i depend on bias voltages. For given high-frequency current–voltage characteristics calculated by the physical HEMT model (Section II-A), g_m and G_{ds} can be evaluated at any bias using

$$g_m = dI_{ds}/dV_g \quad (25a)$$

$$G_{ds} = dI_{ds}/dV_{ds}. \quad (25b)$$

The same applies to C_{gs} and C_{dg}, which can be derived from the high-frequency charge–voltage characteristics presented in Section II-B:

$$C_{gs} = dQ/dV_{gi} \quad (26a)$$

$$C_{dg} = dQ/dV_{gdi}. \quad (26b)$$

V_{gi} is the intrinsic gate–drain voltage and V_{gdi} the intrinsic gate–drain voltage.

The transit time τ is evaluated by integrating the velocity along the channel:

$$\tau = \int_{z=0}^{L_g} (1/v)\, dz \quad (27a)$$

$$= (Wq/I_d)\int_{V_e(0)}^{V_e(L_1)} n_s(V_e)(dz/dV_e)\, dV_e + L_2/v_s. \quad (27b)$$

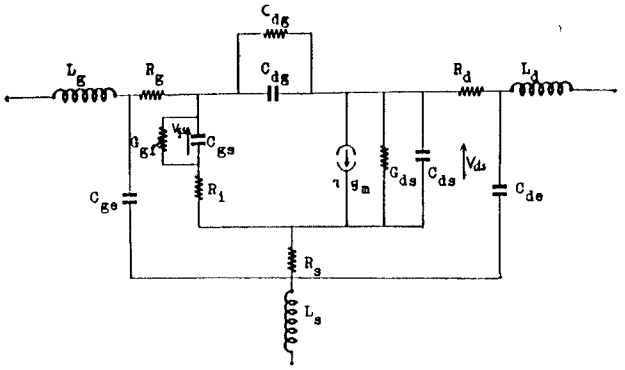

Fig. 3. High-frequency equivalent circuit used to predict HEMT small- and large-signal characteristics.

The following procedure was applied in order to model the HEMT high-frequency characteristics based on physical parameters:

1) Determine the current–voltage characteristics from (13) at operation-representative bias points. Add the substrate current according to (15) and (16). Set R_s, R_d to zero in order to calculate the intrinsic currents and voltages.

2) Evaluate the charge–voltage characteristics at the bias points of step 1 using (22) or (24).

3) To obtain the g_m and G_{ds} voltage-dependent characteristics, determine the fitting parameters of the equations following below ((28a)–(28c)), so that the difference between physically calculated characteristics and obtained results is minimum. G_{ds} and g_m can then also be found as a function of intrinsic bias:

$$I_{ds}(V_d,V_g)=I_{d0}\left(f'\tanh(P_1V_d)+P_2V_d\right)$$
$$f'=u*v \qquad P_1=a_1+a_2V_g+a_{15}V_g^2$$
$$P_2=a_3+a_8V_g \qquad u=V_{gs}^g$$
$$v=\frac{1}{c_1+c_2V_{gs}^2+c_3V_{gs}^4}$$
$$g=2+a_{10}+a_{14}V_d \qquad V_{gs}=V_g+V_T$$
$$c_1=1+a_5+a_7V_d \qquad c_2=a_4+a_{11}V_d$$
$$c_3=a_{12}+a_{13}V_d \qquad V_T=a_6+a_9V_d$$
$$I_{d0}=100\text{ mA} \tag{28a}$$

$$g_m(V_d,V_g)=\frac{\partial I_{ds}}{\partial V_g}=I_{d0}\left(\frac{\partial f'}{\partial V_g}\tanh(P_1V_d)+\frac{f'P_1'V_d}{\cosh^2(P_1V_d)}+P_2'V_d\right)$$
$$\frac{\partial f'}{\partial V_g}=u'v+v'u \qquad u'=gV_{gs}^{(g-1)}$$
$$v'=-\frac{2c_2V_{gs}+4c_3V_{gs}^3}{\left(c_1+c_2V_{gs}^2+c_3V_{gs}^4\right)^2}$$
$$P_1'=a_2+2a_{15}V_g, \qquad P_2'=a_8 \tag{28b}$$

$$G_{ds}(V_d,V_g)=\frac{\partial I_{ds}}{\partial V_g}=I_{d0}\left(\frac{\partial f'}{\partial V_d}\tanh(P_1V_d)+\frac{f'P_1}{\cosh^2(P_1V_d)}+P_2\right)$$
$$\frac{\partial f'}{\partial V_g}=u'v+v'u \qquad u'=\left(g'\ln(V_{gs})+\frac{gV_T'}{V_{gs}}\right)V_{gs}^g$$
$$v'=-\frac{c_1'+c_2'V_{gs}^2+2c_2V_T'V_{gs}+c_3'V_{gs}^4+4c_3V_T'V_{gs}^3}{\left(c_1+c_2V_{gs}^2+c_3V_{gs}^4\right)^2}$$
$$c_1'=a_7 \qquad c_2'=a_{11} \qquad c_3'=a_{13}$$
$$V_T'=a_9 \qquad g'=a_{14}. \tag{28c}$$

4) The C_{gs} and C_{dg} voltage-dependent characteristics can similarly be obtained by fitting the following functions to physically calculated charge–voltage characteristics:

$$Q(V_d,V_g)=Q_0\left\{f'(x_1+x_2)^2+g\right\}$$
$$f'=a_3+a_4x_1+a_9x_1^2 \qquad g=Q_1Q_2$$
$$x_1=V_g \qquad x_2=V_d-V_g$$
$$Q_1=a_1+a_2x_1+a_5x_1^2 \qquad Q_2=a_6+a_7x_2+a_8x_2^2$$
$$Q_0=100\text{ fC} \tag{29a}$$

$$C_{gs}(V_d,V_g)=-\frac{\partial Q}{\partial V_g}=-Q_0\left\{\frac{\partial f'}{\partial x_1}(x_1+x_2)^2+2f'(x_1+x_2)+\frac{\partial g}{\partial x_2}\right\}$$
$$\frac{\partial f'}{\partial x_1}=a_4+2a_9x_1 \qquad \frac{\partial g}{\partial x_1}=Q_1'Q_2$$
$$Q_1'=a_2+2a_5x_1 \tag{29b}$$

$$C_{dg}(V_d,V_g)=\frac{\partial Q}{\partial V_{dg}}=Q_0\left\{2f'(x_1+x_2)+\frac{\partial g}{\partial x_2}\right\}$$
$$\frac{\partial g}{\partial x_2}=Q_2'Q_1 \qquad Q_2'=a_7+2a_8x_2. \tag{29c}$$

IV. Validity of the Model

The validity of the model described in the previous sections was tested by applying it to HEMT's fabricated in our laboratory. Fig. 4 shows measured and modeled dc characteristics for such devices. The latter are plotted using the fitting functions of (28). The nominal physical parameter values are listed together with those used for modeling in Table I. A good agreement can in general be observed apart from the thickness of the AlGaAs layer, which had to be reduced in order to predict correctly the smaller measured pinch-off voltage.

A good agreement is also shown between measured and modeled I–V current curves (see Fig. 4). The differences observed at small drain voltages and near pinch-off operation are mainly due to the approximations made in modeling the substrate current (eqs. (14), (15)).

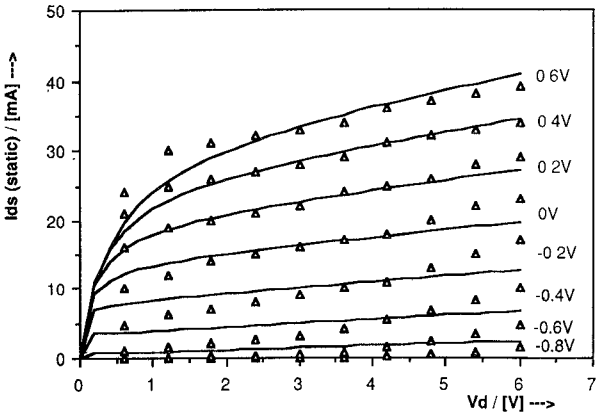

Fig. 4. Comparison of measured (△) and predicted (——) HEMT I–V characteristics of a 150 μm×0.6 μm device.

TABLE I
PHYSICAL PARAMETERS USED FOR HEMT MODELING
(NOMINAL VALUES GIVEN IN PARENTHESES)

W / [μm]	150	(150)
L_g / [μm]	0.6	(0.6)
d_o / [Å]	545	(900)
d_i / [Å]	22	(22)
N_d / [m^3]	6 x 10^{23}	(7 x 10^{23})
x / [%]	22	(22)
v_s/ [m/s]	1.25 x 10^5	
F_c/ [V/m]	3.2 x 10^5	
μ/[m^2/(Vs)]	0.69	
k_o/[V/[Am^2]	3.75 x 10^{16}	
k_n/[S m]	5.35 x 10^8	
k_h/[S m]	1 x 10^9	
V_p/[V]	-0.74	(-0.75)

Fig. 5 shows extrinsic modeled g_m characteristics together with those obtained from S-parameter measurements performed at different bias voltages in the 2–18 GHz frequency range. The g_m values were obtained using measured R_s, R_d data. The g_m–V_g dependence is correctly modeled, and predicts a maximum g_m at about $V_g = 0$ V and g_m compression for increasingly high positive gate bias. This g_m compression is considered in the physical model by the saturated electron gas concentration characteristics. The g_m–V_{ds} dependence is more difficult to predict accurately with theory, since it is also influenced by substrate currents. Fig. 4 shows, however, that the linear approximation made in Section II-A for the substrate conductance is accurate for drain voltages corresponding to saturated device characteristics.

Fig. 6 shows modeled gate capacitance C_{gs} bias dependence together with the results of high-frequency S-parameter measurements. The overall agreement is again reasonable in spite of the approximations made in the

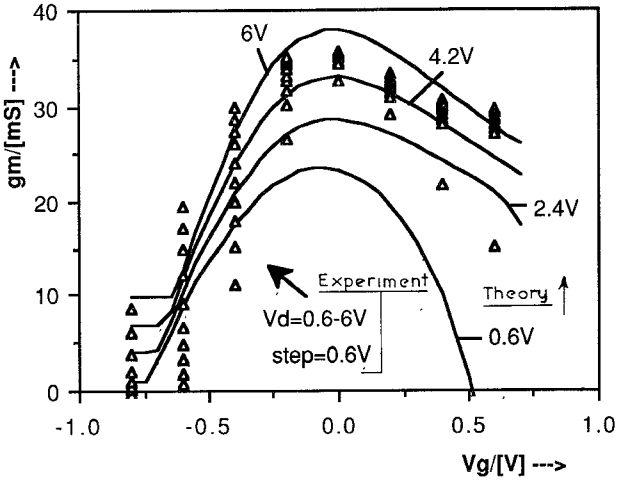

Fig. 5. Comparison of measured (△) and predicted (——) g_m versus voltage characteristics of a 150 μm×0.6 μm HEMT.

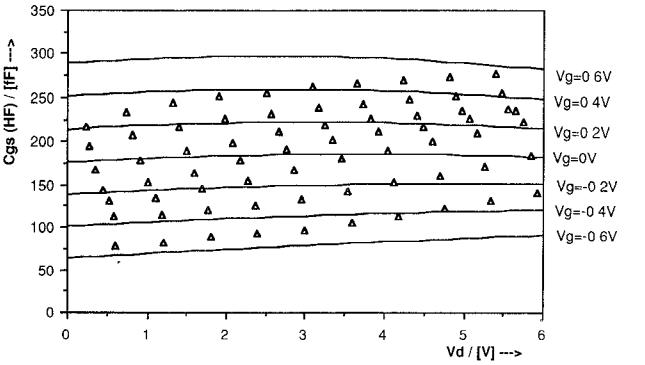

Fig. 6. Comparison of measured (△) and predicted (——) C_{gs}-voltage characteristics of a 150 μm×0.6/μm HEMT.

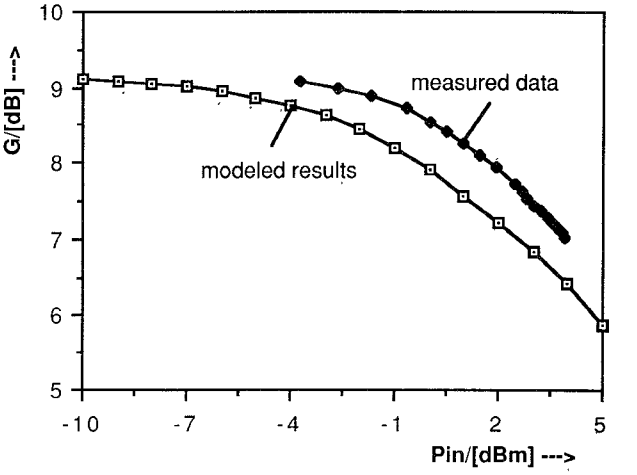

Fig. 7. Comparison of experimental and predicted gain saturation of a 150 μm×0.6 μm HEMT terminated with 50 Ω at input and output ($V_d = 5$ V, $V_g = 0$ V, $f = 8$ GHz).

physical model. Since the physical model predicts the bias dependence of the principal HEMT nonlinearities, it can also be used to predict its large-signal behavior [12], [14]. Fig. 7 shows gain (G) versus input power (P_{in}) characteris-

tics of a HEMT as obtained from physical modeling and experimental characterization under 50-Ω terminations. The choice of 50-Ω terminations was necessary in order to ensure measurement reproducibility and avoid simulation inaccuracies due to incorrectly determined loads. The small-signal gain agrees within 1 dB, while the output power is underestimated by about 2 dBm. These differences arise mainly from the approximations made in the physical modeling of substrate current.

V. Dependence of Large Signal Characteristics on Physical Parameters

The physical model described here can be used to predict qualitatively the influence of physical parameters on small- and large-signal HEMT characteristics. The following discusses the influence of gate length L_g, AlGaAs thickness d_0, spacer-layer thickness d_i, and doping density N_d on the nonlinear HEMT behavior. The results have been obtained by the method of nonlinear analysis described in [13] and [14].

A. Influence of Gate Length on Output Power

Varying the gate length of a HEMT influences its effective saturation velocity v_s [22]. Here the following empirical formula is used to predict saturation velocities:

$$v_s(L_g) = \frac{v_s(L_g = 1\ \mu\text{m})}{\sqrt{L_g[\mu\text{m}]}}. \tag{30}$$

The variation of the saturation velocity v_s with gate length can arise by velocity overshoot.

The parasitic R_s, R_d resistances were determined using the distributed line technique described by Weiler [8] and Berger [20]. Unsaturated and saturated velocity-field characteristics were used for R_s and R_d calculations, respectively. Fig. 8 shows the frequency dependence of the saturated output power at 1 dB gain compression for three different gate lengths. All calculations were performed by considering the basic frequency only. If higher harmonic signal components are to be considered, the principal frequency of analysis should be limited to smaller values, since the equivalent circuit shown in Fig. 3 is not valid for "high-harmonic" frequencies larger than 30 GHz.

The drain bias was chosen for optimum power added efficiency for each gate length at 10 GHz. The gate bias was selected for maximum output power operation by setting $V_g = V_g(I_{\max}/2)$. ($I_{\max}$ is the maximum HEMT drain–source current.) In the case of large gate-forward bias V_{gsf}, the gate current I_{gsf} can in practice become higher than 1 percent of the $I_{\max}$ value. The maximum allowed operating drain–source current was then set to a value I_F corresponding to the limiting gate voltage V_{gsf}.

Large gate lengths provide high output powers at small frequencies. As expected, the highest gain is obtained with HEMT's having shorter gate lengths. The decrease of output power with gate length at low frequencies results from the associated gain and gate resistance increase. The larger power drop observed by reducing the gate length from 0.6 μm to 0.3 μm is due to the higher effective length change $\Delta L/L$. An opposite tendency is shown at high frequencies, where the power is increased by reducing the gate length. This comes from the fact that the comparison is made at −1 dB compression of the gain available at each frequency; at high frequencies the large gate devices do not have any useful gain and consequently power.

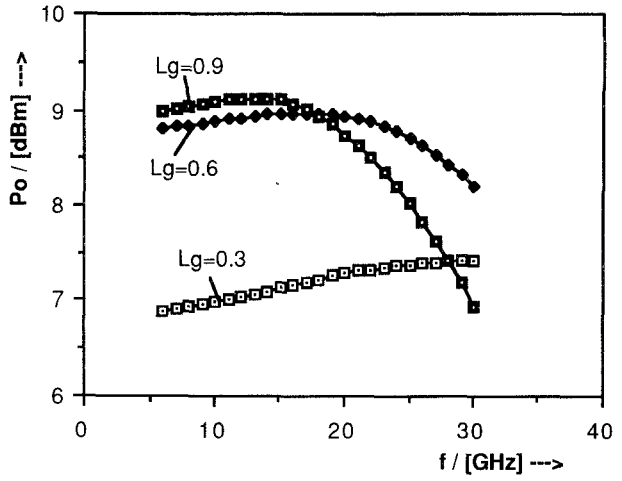

Fig 8. P_o versus frequency characteristics at 1 dB gain compression as a function of frequency f and gate length L_g. Input impedance: 50 Ω. Output impedance: matched at small-signal level.

B. Influence of the Doped AlGaAs Layer Thickeness d_0 on Output Power

Changing the thickness d_0 implies a change of gate–drain avalanche characteristics due to variation of the undepleted charge per unit area Q_u of the AlGaAs layer. Using Wemples's [15] and Frensley's [16] theory for calculating Q_u and the gate breakdown voltage V_b of HEMT's, one has

$$V_b = B/(d_0 N_d) \qquad B = 4.4\times10^{+17}\ [\text{V/m}^2]. \tag{31}$$

The value of B was obtained by modifying Frensley's theory in order to account for the modified dielectric constant of the AlGaAs.

Avalanche current was modeled using a simple diode-type exponential expression as suggested by Materka [17]:

$$I_{gd} = I_{g0}\left[\exp(cV_{gd}) - 1\right] \tag{32}$$

where I_{g0} is the reversed diode current, V_{gd} is the operating gate–drain voltage, and c is a heuristic constant relating the diode breakdown voltages V_b to the I_{gd}–V_{gd} characteristics of (32):

$$c = \left[\ln\left(I_{\max}/(100\ I_{g0}) + 1\right)\right]/V_b. \tag{33}$$

Fig. 9(a) shows the drain-voltage dependence of the output power and power added efficiency at 1 dB gain compression for different d_0. The output power increases with d_0 and saturates at high V_{ds}. The power increase with V_{ds} is due to smaller effective g_m and larger G_{ds} values for

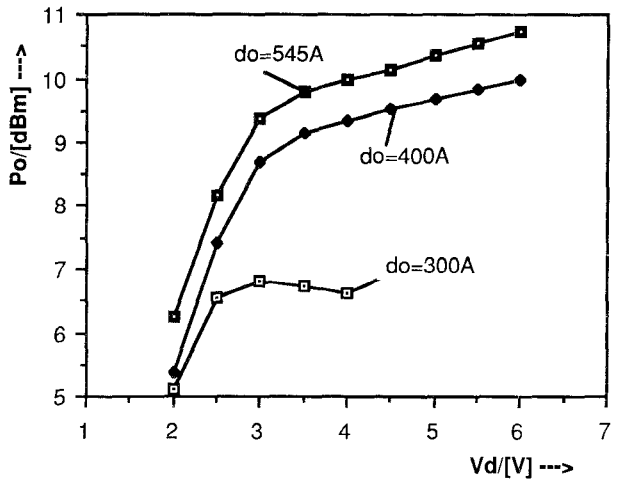

Fig. 9. Dependence of (a) output power P_o at 1 dB gain compression and (b) power added efficiency PAE at 1 dB gain compression on AlGaAs layer thickness d_0 and drain bias V_d (input impedance: 50 Ω; output impedance: matched at small-signal level).

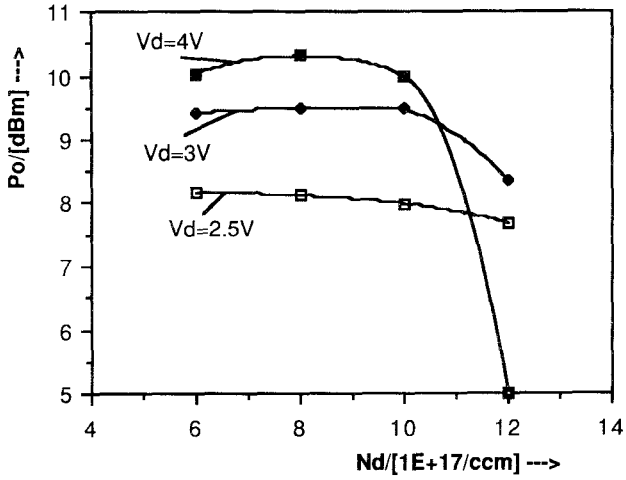

Fig. 10. Dependence of output power P_o at 1 dB gain compression on AlGaAs doping N_d and drain bias V_d (input impedance: 50 Ω; output impedance: matched at small-signal level).

operation away from the linear region. The change of d_0 will shift the gate bias operating range, and is accompanied by a power increase. At small d_0 values, pinch-off occurs near zero or even positive V_{gs}. The HEMT is therefore biased in a region where the gate–source diode results in large forward currents, and output power is limited. Larger d_0's imply large negative pinch-off voltages and therefore smaller influence of the partially forward operated diode. When d_0 exceeds 500 Å, the HEMT operates far from the limiting diode-forward current region and other saturation mechanisms such as g_m compression are more important. Any further d_0 increases will lead to even larger pinch-off voltages. The output power is, however, this time not increasing any further, because it is dictated by the g_m nonlinearity.

Fig. 9(b) shows that the power added efficiency of HEMT's is maximum at a certain V_{ds} value. As confirmed from Fig. 9(a), this occurs at the point of output power saturation with V_{ds}. At drain bias higher than this point, the output power shows only small increases. At the same time, the dc power increases proportionally to V_{ds}, with the net result of a reduced power added efficiency [21].

The power added efficiency decreases finally with d_0, due to an increase of dc current. The latter implies large dc powers and small power added efficiencies.

C. Influence of AlGaAs-Layer Doping N_d

Fig. 10 shows the output power at 1 dB gain compression as a function of AlGaAs doping density N_d. N_d variations change the parasitic access resistances and modify the gate–drain avalanche characteristics. The first have been calculated as described in Section V-A and the latter were evaluated according to (32). V_g bias voltages have been determined by optimizing the output power as described earlier (Section V-A).

At large V_{ds}, the output power increases initially with doping because of the larger associated currents and pinch-off voltages. Larger input voltage swings may therefore be allowed before saturation due to g_m decrease. When N_d is larger than a certain limit (here: $N_d = 10^{17}/\text{cm}^3$), the output power starts decreasing with doping due to the importance of gate–drain avalanche.

D. Influence of Spacer Layer Thickness

Fig. 11 shows HEMT output power as a function of V_g for three different spacer layers. The output power is initially increasing with V_g. At V_g's exceeding 0.0 V, this increase starts taking place at a smaller P_0/V_g rate. The $V_g = 0.0$ V operation corresponds, as a matter of fact, to a bias for maximum g_m. At very high gate bias, the output power is finally decreasing because of partial forward operation of the gate–source diode.

Fig. 11 shows also that the power can decrease with increasing spacer thickness d_t. This effect is explained by

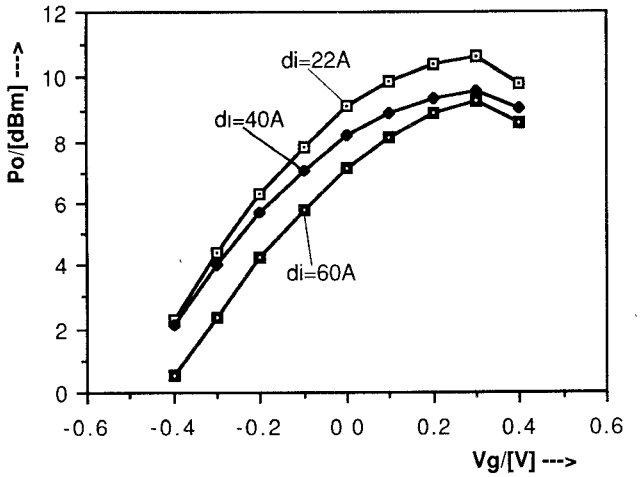

Fig. 11. Dependence of output power P_o at 1 dB gain compression on spacer layer thickness d_i and gate bias V_g (input impedance: 50 Ω; output impedance: matched at small-signal level).

the lower electron gas concentrations when d_i is large. Such an effect is not, however, very pronounced in practice due to the accompanying mobility increase, which improves the output power.

VI. Conclusions

A simple, one-dimensional physical HEMT model has been shown to predict satisfactorily the small- and large-signal characteristics of transistors with submicron gate lengths. The analysis includes the calculation of parasitic capacitances and the evaluation of substrate leakage currents. The model uses an interpolation function for the E_f versus n_s HEMT characteristics which can be fitted to a large variety of numerical results and allow analytical problem solution.

The use of the model in large-signal analysis allows one to determine the influence of device physical parameters on power operation. The model predicts an optimum gate length for maximum output power at a given frequency of operation. The power levels increase with the doped layer thickness d_0 up to a maximum value of $d_0 = 500$ Å. At high V_{ds} bias, the output powers increase with doping density until gate–drain avalanche initiates early saturation. Large spacer layer thicknesses are predicted to decrease the available output power.

Appendix I
Evaluation of Parameters Necessary for the Calculation of n_s–V_e Characteristics

The constants $a, b, \cdots$ can be evaluated by using (5) together with the charge-control model proposed by Delagebeaudeuf [1]:

$$qn_s = V_{fi} - V_g + V_d(z) + E_f - \Delta E_c - \frac{qN_d d_0^2}{2\varepsilon_2}. \quad \text{(A1)}$$

The coefficients a_i fitting (5) to characteristics of triangular-well calculations are as follows:

$$a_0 = -0.1101912 \qquad a_1 = 2.3396118\times10^{-2}$$
$$a_2 = 1.2039864\times10^{-2} \qquad a_3 = 7.127383\times10^{-1}. \quad \text{(A2)}$$

Solving (5) together with (A1) for n_s,

$$fn_s = -\frac{a_3 qd_0/(f\varepsilon_2) - V_e + a_1}{2(qd_0/(f\varepsilon_2) + a_2)} - \sqrt{\left\{\frac{(a_3 qd_0/(f\varepsilon_2) - V_e + a_1)^2}{4(qd_0/(f\varepsilon_2) + a_2)^2} - \frac{a_0 - V_e a_3}{qd_0/(f\varepsilon_2) + a_2}\right\}} \quad \text{(A3)}$$

with

$$V_e = \Delta E_c - V_{fi} + V_g + qN_d d_0^2/(2\varepsilon_2) - V_d(z). \quad \text{(A4)}$$

Coefficients $a_0, \cdots, a_3$ are given in (A2). Equation (A3) is valid until n_s starts to saturate at a voltage where $n_s = pn_{s0}$ (n_{s0} is the equilibrium concentration given by [1] and p is arbitrarily chosen to $p = 0.75$). At $V_e = V_{e1}$, $n_s = pn_{s0}$ and (A3) is replaced by

$$fn_s = c_0 + c_1 V_e + c_2 V_e^2. \quad \text{(A5)}$$

The coefficients $c_0 \cdots c_2$ are determined such that the polynomial of (A5) has 1) its maximum for $n_s = n_{s0}$, 2) a value equal to pn_{s0} at the boundary with the curve described by (A3), and 3) equal slopes at this boundary. Further, at $V_e = V_{e1}$, the results of (A3) and (A5) are smoothly connected to each other. For $A = n_s(V_{e1})$ and $B = dn_s/dV_e$ at $V_e = V_{e1}$, the coefficients $c_0 \cdots C_2$ are

$$c_0 = A - BV_{e1} + \frac{BV_{e1}}{4(A - fn_{s0})} \quad \text{(A6a)}$$

$$c_1 = B - \frac{2B^2 V_{e1}}{4(A - fn_{s0})} \quad \text{(A6b)}$$

$$c_2 = \frac{B}{4(A - fn_{s0})} \qquad A = n_s(V_{e1})$$
$$B = dn_s/dV_e|_{V_e = V_{e1}} \qquad f = 10^{-15}. \quad \text{(A6c)}$$

V_{e1} is evaluated with (10a) by setting n_s to pn_{s0}:

$$V_{e1} = (pfn_{s0})qd/(f\varepsilon_2) + \frac{a_0 + a_1(pfn_{s0}) + a_2(pfn_{s0})^2}{(pfn_{s0}) + a_3},$$
$$p = 0.75. \quad \text{(A7)}$$

The complete relation between n_s and V_e is obtained by summarizing (A3) and (A5). It is given in (3) when using

the following expressions for the constants $a, b, \cdots$:

$$a = \frac{a_3 qd/(f\varepsilon_2) + a_1}{2(qd/(f\varepsilon_2) + a_2)} \qquad b = \frac{1}{2(qd/(f\varepsilon_2) + a_2)}$$

$$c = \frac{-2a_0}{b}$$

$$\beta = 2ab + a_3/\{qd/(f\varepsilon_2) + a_2\} \qquad \gamma = a^2 + c. \quad \text{(A8)}$$

V_{e2} is finally the turn-on potential for electron gas modulation.

Appendix II
Evaluation of Integrals Necessary for Current and Charge Modulation

1) Evaluation of the Current Integral $\int_{V_{eb}}^{V_{ea}} n_s\, dV_e$:

$$\int_{V_{eb}}^{V_{ea}} n_s\, dV_e = -\int_{V_{ea}}^{V_{eb}} n_s\, dV_e$$

$$= \begin{cases} -n_{s0}(V_{eb} - V_{ea}) & V_{eb} < V_{e2} \\ I_0 + g_1(V_{eb}) - g_1(V_{e2}) & V_{e2} < V_{eb} < V_{e1} \\ I_1 + g_2(V_{eb}) - g_2(V_{e1}) & V_{e1} < V_{eb} \end{cases} \quad \text{(A9)}$$

where $V_{e2} = -c_1/2c_2$ is the turn-on potential for electron gas modulation and

$$g_1(x) = c_0 x + c_1 x^2/2 + c_2 x^3/3 \quad \text{(A10)}$$

$$g_2(x) = ax + bx^2/2 + h_1(x) + h_2(x) \quad \text{(A11)}$$

$$h_1(x) = \frac{(2b^2x + \beta)(b^2x^2 + \beta x + \gamma)^{1/2}}{4b} \quad \text{(A12)}$$

$$h_2(x) = \frac{\ln\left\{2\left[b(b^2x^2 + \beta x + \gamma)\right]^{1/2} + 2b^2x + \beta\right\}}{8b^3} \quad \text{(A13)}$$

$$I_0 = \int_{V_{ea}}^{V_{e2}} n_s(V_e)\, dV_e \quad \text{for} \quad V_{ea} > V_{e2} \quad \text{or}$$

$$I_0 = 0 \quad \text{for} \quad V_{ea} < V_{e2} \quad \text{(A14)}$$

$$I_1 = \int_{V_{ea}}^{V_{e1}} n_s(V_e)\, dV_e \quad \text{for} \quad V_{ea} > V_{e1} \quad \text{or}$$

$$I_1 = 0 \quad \text{for} \quad V_{ea} < V_{e1}. \quad \text{(A15)}$$

Coefficients $a, b, c_0, \cdots, c_2$, and γ are derived in (A6)–(A8).

2) Evaluation of Q_{ns} *Charge Integral:* The Q_{ns} charge integral is solved using the following equations:

$$\int_{V_e(L_0)}^{V_e(L_1)} n_s(z)(dz/dV_e)\, dV_e$$

$$= \begin{cases} -Wq\mu\{g_2[V_e(L_1)] - g_3[V_e(L_0)]\}/I_d - I_A/F_0 \\ \quad \text{for } V_e(L_1) > V_{e1} \\ -Wq\mu\{I_3 + g_4[V_e(L_1)] - g_4[V_{e1}]\}/I_d - I_A/F_0 \\ \quad \text{for } V_e(L_1) \leq V_{e1} \end{cases} \quad \text{(A16)}$$

with

$$g_3(V) = \frac{(c_0 + c_1 V)^3}{3c_1} + \frac{2c_0c_2}{3}V^3 + \frac{c_1c_2}{2}V^4 + \frac{c_2^2}{5}V^5 \quad \text{(A17)}$$

$$g_4(V) = h_3(V) + h_4(V) \quad \text{(A18)}$$

$$h_3(V) = \frac{(a + bV)^3}{3b} + \frac{b^2}{3}V^3 + \frac{\beta}{2}V^2 + \gamma V \quad \text{(A19)}$$

$$h_4(V) = (2a - \beta/b)(h_1(V) + h_2(V)) + 2(b^2V^2 + \beta V + \gamma)^{3/2}/(3b) \quad \text{(A20)}$$

$$I_A = \int_{V_e(L_0)}^{V_e(L_1)} n_s\, dV_e \qquad I_3 = g_3[V_{e1}] - g_3[V_e(L_0)]. \quad \text{(A21)}$$

In case of $V_e(L_g) > V_{e1}$, I_3 becomes zero and V_{e1} has to be replaced by $V_e(L_g)$ in (A21). The expressions for h_1 and h_2 are given in (A12) and (A13). The coefficients $c_0, \cdots, c_2$ are defined in (A6), and parameters a, b, c, and γ can be obtained with (A8).

References

[1] D. Delagebeaudeuf and N. T. Linh, "Metal-(n) AlGaAs-GaAs two-dimensional electron gas FET," *IEEE Trans. Electron Devices*, vol. ED-29, pp. 955–960, June 1982.

[2] D. Delagebeaudeuf, P. Delescluse, M. Laviron, N. Tung, J. Chaplart, J. Chevrier, and N. T Linh, "Low and high field transport properties in two-dimensional electron gas FET," Inst. Phys. Conf. Ser. No. 65, ch. 5, pp. 393–397; paper presented at the Int. Symp GaAs and Related Compounds, Albuquerque, 1982.

[3] T. J. Drummond, H. Morkoc, K. Lee, and M. Shur, "Model for modulation doped field effect transistors," *IEEE Electron Device Lett.*, vol. EDL-3, pp. 338–341, Nov. 1982

[4] K. Lee, M. S Shur, T. J Drummond, and H. Morkoc, "A unified method for characterizing (Al,Ga)As/GaAs MODFET's including parasitic MESFET conduction in the (Al,Ga)As," in *Proc 4th Cornell Conf.*, 1983, pp. 177–186.

[5] K. Park and K. D. Kwack, "A model for the current-voltage characteristics of MODFET's," *IEEE Trans. Electron Devices*, vol. ED-31, pp. 29–35, Jan. 1984.

[6] T. Mimura, K. Joshin, and S. Kuroda, "Device modeling of HEMT's," *Fujitsu Sci. Tech. J.*, vol. 19, no 3, pp 243–278, Sept. 1983.

[7] P. Saunier and J. W. Lee, "High-efficiency millimeter-wave GaAs/GaAlAs power HEMT's," *IEEE Electron Device Lett.*, vol. EDL-7, pp. 503–505, Sept. 1986.

[8] M H. Weiler and Y. Ayasli, "DC and microwave models for $Al_xGa_{1-x}As/GaAs$ high electron mobility transistors," *IEEE Trans. Electron Devices*, vol. ED-31, pp 1854–1861, Dec. 1984.

[9] H. Rohdin and P. Roblin, "A MODFET dc model with improved pinchoff and saturation characteristics," *IEEE Trans Electron Devices*, vol. ED-33, May 1986.

[10] D. J. Arnold, R. Fischer, W. F Kopp, T S. Henderson, and H Morkoc, "Microwave characterization of (Al,Ga)As/GaAs modulation-doped FET's: Bias dependence of small-signal parameters," *IEEE Trans. Electron Devices*, vol. ED-31, pp. 1399–1402, Oct. 1984.

[11] D. Arnold, W. Kopp, R. Fischer, J Klem, and H. Morkoc, "Bias dependence of capacitances in modulation doped FET's at 4 GHz," *IEEE Electron Device Lett.*, vol. EDL-5, pp. 123–125, Apr. 1984.

[12] M. Weiss and D. Pavlidis, "Power optimization of GaAs implanted FET's," *IEEE Trans. Microwave Theory Tech.*, vol. MTT-35, pp. 175–188, Feb. 1987.
[13] M. Weiss and D. Pavlidis, "A comparative study of TEGFET and MESFET large signal characteristics and saturation mechanisms," in *Proc. IEEE MTT-S-Conf.*, Las Vegas, 1987 pp. 553–556.
[14] M. Weiss and D. Pavlidis, "An investigation of power characteristics and saturation mechanisms in HEMT's and MESFET's," submitted for publication.
[15] W. H. Wemple, W. C. Niehaus, H. M. Coe, J. V. Dilorenzo, and W. O. Schlosser, "Control of gate–drain avalanche in GaAs MESFET's," *IEEE Trans. Electron Devices*, vol. ED-27, pp. 1013–1018, June 1980.
[16] W. R. Frensley, "Power-limiting breakdown effects in GaAs MESFET's," *IEEE Trans. Electron Devices*, vol. ED-28, pp. 962–970, Aug. 1981.
[17] A. Materka and T. Kacprzak, "Computer calculation of large-signal GaAs FET amplifier characteristics," *IEEE Trans. Microwave Theory Tech.*, vol. MTT-33, pp. 129–135, Feb. 1985.
[18] T. Takada, K. Yokoyama, M. Ida, and T. Sudo, "A MESFET variable-capacitance model for GaAs integrated circuit simulation," *IEEE Trans. Microwave Theory Tech.*, vol. MTT-30, pp. 719–724, May 1982.
[19] T.-H. Chen and M. S. Shur, "A capacitance model for GaAs MESFET's," *IEEE Trans. Electron Devices*, vol. ED-32, pp. 883–891, May 1985.
[20] H. H. Berger, "Contact resistance in diffused resistors," in *IEEE Solid-State Circuits Conf. 1969: Dig. Tech. Papers*, pp. 160–161.
[21] D. Pavlidis, G. Ng, H. F. Chau, M. Weiss, J. Hu, and W. P. Hong, "Electronic properties of power high electron mobility transistors," presented at Conf. Ballistic Electrons for Transistors, Santa Barbara, CA, March 22–27, 1987.
[22] J.-L. Cazaux, "Analyse des Proprietes Electriques du Transistor a Effet de Champ en Arseniure de Gallium a Profil de Dopage non uniforme," Doctors thesis, Institut National des Sciences Appliquees de Toulouse, Toulouse, France, 1985.

✠

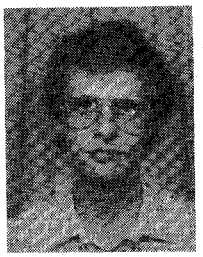

Matthias Weiss (S'87) was born in Kassel, West Germany, in December 1958. He received the Diplom (master's degree) in electrical engineering at the Technische Hochschule Darmstadt, Darmstadt, West Germany, in 1984.

During his studies, he worked at Thomson C.S.F., France, on monolithic microwave broadband amplifiers in the 2–10 GHz frequency range and at the Theoretische Elektrotechnik Institute of the Technical University Darmstadt on the theoretical investigation of waveguides. From 1984 to 1987, he was a researcher at Thomson Semiconducteurs, Orsay, France, working towards the Ph.D. degree on MESFET and HEMT large-signal properties. In 1987 he joined the Department of Electrical Engineering and Computer Science at the University of Michigan, Ann Arbor. He is currently completing the Ph.D. degree.

✠

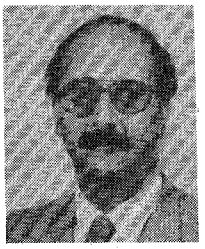

Dimitris Pavlidis (S'73–M'76–SM'83) was born in Athens, Greece, in 1950. He received the B.Sc. degree in physics from the University of Patras, Greece, in 1972 and the Ph.D. dgree in applied science–electronic engineering from the University of Newcastle-upon-Tyne, England, in 1976.

From 1975 to 1978 we worked as a Postdoctoral Fellow at the Department of Electrical and Electronic Engineering of Newcastle University. In 1978 he joined the High Frequency Institute of the Technical University of Dermstadt, West Germany. In 1980 he worked for UNESCO as consultant at the Central Electronic Engineering Research Institute, Pilani, India. During the years 1980–1985 he was Engineer and Manager of the GaAs Monolithic Microwave Integrated Circuits (MMIC) Group of Thomson-CSF DHM/DAG, Corbeville, France. In 1986 he was appointed Professor of Electrical Engineering and Computer Science at the University of Michigan, Ann Arbor. His current research interests cover the design and fabrication of HEMT's, HBT's, III–V microwave and millimeter devices and IC's.

Dr. Pavlidis's publications are in the area of microwave semiconductor devices and circuits. He holds six patents on MMIC applications. He was chairman of the 7th European Specialist Workshop on Active Microwave Semiconductor Devices (AMSD), Spetsai, Greece, 1981, and Secretary of the 11th International Symposium on GaAs and Related Compounds, Biarritz, France, 1984.